Viscous fingering in a wedge

Martine Ben Amar
Laboratoire de Physique Statistique, Ecole Normale Supérieure, 24 rue Lhomond, 75231 Paris CEDEX 05, France
(Received 7 January 1991)

The selection of self-similar fingers growing in a wedge is examined numerically both in the convergent and divergent flow regime. For divergent flows, a bifurcation occurs in the spectrum of the relative finger width λ versus σ, the effective surface tension parameter, when it is very small ($\sigma < 0.005$). By comparison with experimental data, we show that it can explain the tip-splitting instability usual to any radial growth process. At finite surface tension ($\sigma > 0.005$), a universal selection law is revealed numerically for any sector value, in both growth regimes.

I. INTRODUCTION

Viscous fingering in a wedge was introduced in a recent experiment [1]. Initially the aim was to understand the dynamical evolution of viscous patterns in radial growth, i.e., what is known now as the Bataille-Paterson geometry [2]. Although fairly common in nature, radial growth phenomena have been neglected, to some extent, by theorists in hydrodynamics. However, recently, this growth process has suggested several statistical approaches [1,3]. Several aspects remain unexplained at present like the destabilization of the pattern by tip-splitting or the crossover between petal and dendritic shapes for crystal seeds. The sector geometry is an intermediate step between the very well-established linear geometry developed by Saffman and Taylor [4] and the completely open one. The main advantage of traditional experiments in a linear channel is to produce steady fingers with a constant velocity. For a long time, the major problem has been to understand the observed value for the relative width λ of the experimental finger [5] whereas Saffman and Taylor (ST) [4] have shown the existence of a possible continuum set of symmetric solutions with every possible λ. It is now well established, by analytical [6] or numerical means [7], that a tiny isotropic surface tension selects the solution which tends to occupy half the channel. In fact, an infinite discrete set is selected but only the finger with the lowest λ value is linearly stable [8].

In an open geometry, steady solutions no longer exist even if the imposed fluid flux is time independent. In sector shaped cells of angle θ_0, the experiments are performed, usually at constant applied pressure. Even though the effective surface tension σ is not constant in this condition, a growth regime of nearly smooth and self-similar fingers is observed. These fingers are characterized by the ratio λ of their angular width to θ_0. This suggests [1,9,10] that the dynamic is slow enough so the finger has time to adjust its shape to the corresponding ideal self-similar finger. This would be the starting point for a theoretical treatment and we address the question of the selection mechanism via an effective surface tension parameter σ of self-similar patterns, for arbitrary value of the wedge angle. It is worth noting that self-similar shapes have also been obtained experimentally by an averaging of very unstable ST fingers and diffusion-limited aggregation (DLA) patterns [11]. This is beyond the scope of the present paper. Hakim has found a continuous family of analytical solutions in the particular case $\theta_0 = 90°$ and Brener *et al.* [10] found a selection criterion at this angle. Experimentally, the fingers at this angle are very unstable so the comparison to theory is limited (the theoretical shape is observed in the averaging of experiments only). More recently the analytical expression for the family of solutions for any value of θ_0 in the absence of surface tension was found [12]. In the present paper, we give two numerical methods leading to the understanding of the selected structures and their stability.

The transformation of the free-boundary problem into an integro-differential equation is standard by now. We show that it can be done either by the Green's-function technique [9,10] or the hodograph method [7,9]. The λ spectrum turns out to be rather unusual: at fixed σ, when the value of the sector grows, the levels meet by pairs to make a series of loops. These loops appear also in the $\lambda = f(\sigma)$ plot, indicating that the self-similar profile disappears when the surface tension becomes arbitrarily small. This phenomenon occurs at rather low surface tension and only for divergent flow. We show here that this explains the dynamical instability in terms of tip-splitting observed in the experiment.

This paper is organized as follows. Section II recalls the equations for the velocity potential either in the viscous fluid and on the interface when three-dimensional effects are neglected. It shows how to transform the physical plane located in a wedge into a fictitious one in a linear channel. Section III establishes the integro-differential equations for the interface, in two different formulations: we want to avoid the study of the fluid flow. Section IV presents the numerical results compared to the experiment [1,9] and previous theoretical treatments [1,3,10,11].

II. THE SELF-SIMILAR FREE-BOUNDARY PROBLEM

A. The viscous fingering equations in the physical plane

When the experiment takes place in a wedge, air can push oil either from the center or from the periphery. In

the first case, the fluid motion is divergent from the center O, in the second it converges toward O. We will try to treat simultaneously these two situations by assigning an algebraic value to the sector angle: positive for divergent flow, negative otherwise. In the physical Π_1 plane, the shape of the interface looks like a petal for divergent flows; for convergent flows, it has the more traditional finger shape. We expect to reach situations for arbitrary value of the sector angle so *a priori* $-2\pi \leq \theta_0 \leq 2\pi$. $\theta_0 = \pm 2\pi$ represents a rather interesting experimental situation of a unique wall crossing a half-space. In the sector, the flow is governed by the Darcy's law valid if the two parallel plates of the cell are closely spaced:

$$\mathbf{v} = -\frac{b^2}{12\mu}\nabla_1 p = \nabla_1 \phi \ . \tag{2.1}$$

p is the pressure, μ the viscosity, and b the distance between the two plates. We have introduced, as usual, the velocity potential which is Laplacian since the fluid is incompressible. The experiment [1] suggests that the interface evolves in times nearly without changing its shape so we will look for self-similar solutions:

$$Y_{\text{int}}(X_1, t) = A(t) y_{\text{int}}\left[\frac{X_1}{A(t)}\right] \ . \tag{2.2}$$

In this particular case, the continuity equation for the velocity, to be applied to the interface, gives

$$n_1 \nabla_1 \phi = R_0^2 A'(t) A(t) \mathbf{n}_1 \cdot \mathbf{r}_1 \ . \tag{2.3}$$

r_1 is a point of the interface at time $t=0$ while X_1 and Y_1 are the coordinates in real space. Here and in the following A' means the first derivative with respect to the natural variable t, while R_0, our length unit, is the position of the nose at time $t=0$. Moreover, the capillary effects fixes the value of the velocity potential for each point of the interface:

$$\phi - \phi_0 = -\frac{b^2}{12\mu}\frac{T}{A(t)R_0}\Omega_1 \tag{2.4}$$

since we have assumed that the pressure P_0 is a constant inside the finger (we neglect air viscosity). Ω_1 is the time-independent curvature and T the surface tension. In the absence of capillary effects, self-similar patterns are dynamical solutions of this free-boundary problem if the experiment is realized with a constant injection or extraction rate:

$$2Q_0 = \int dS_1 \mathbf{v}\cdot\mathbf{n}_1 = R_0^2 A'(t) A(t) \int ds_1 \mathbf{r}_1 \cdot \mathbf{n}_1 \ . \tag{2.5}$$

The flux rate is always positive while the second integral can be either positive or negative following the considered flow regime [see Fig. 1(a) or 1(b)], so we derive, up to a normalization constant,

$$A'(t)A(t) = \pm 1 \ .$$

This implies that the time evolution of the interface is given by $(1+2t)^{1/2}$ for divergent flow, by $(1-2t)^{1/2}$ otherwise. The origin of the time is fixed arbitrarily and we have assumed that time has negative values for the con-

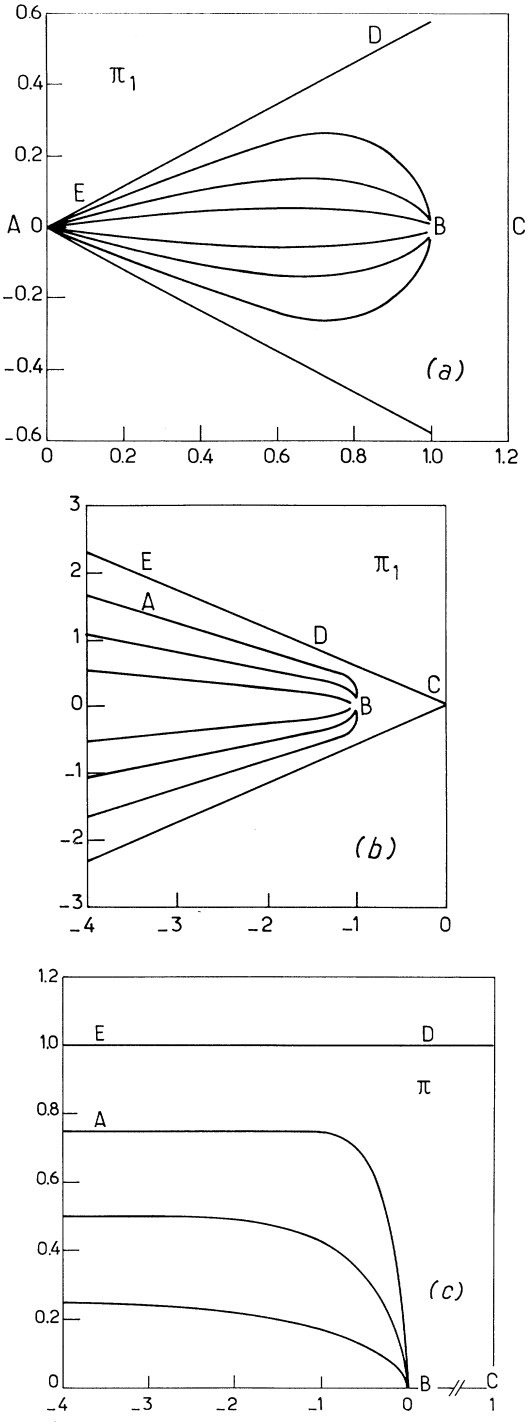

FIG. 1. (a) Self-similar shapes at zero surface tension for a divergent flow corresponding to a sector of $\theta_0 = 60°$. The chosen λ parameter increases from the inner to the outer profile and is equal successively to 0.25, 0.5, and 0.75. (b) Self-similar shapes at zero surface tension for a convergent flow corresponding to a sector of $\theta_0 = -60°$. The chosen λ parameter increases from the inner to the outer profile and is equal successively to 0.25, 0.5, and 0.75. (c) Self-similar shapes at zero surface tension for a divergent flow, after conformal map, corresponding to a sector of $\theta_0 = 60°$. The chosen λ parameter increases from the inner to the outer profile and is equal successively to 0.25, 0.5, and 0.75.

vergent flow regime. The experiment [1] shows regular self-similar patterns only after some times which can be chosen as our time origin. With this choice, the continuity equation [Eq. (2.3)] is time independent, but the Laplace law [Eq. (2.4)] is time dependent so we deduce that adding capillary effects breaks down this class of dynamical self-similar solutions. If one wants to keep the self-similarity which greatly simplifies the analysis of this instability, one must imagine a time-dependent surface tension which of course does not exist. Anyway, if $T/A(t)$ is a slowly varying function, it is reasonable to admit, as in Refs. [1], [9], and [10], that the dynamical pattern is given by a self-similar solution selected by a slowly decreasing surface tension parameter. We will explain some dynamical aspects of the experiment in the last section by assuming this hypothesis, reasonable at long times. As noticed in [10], another way to maintain rigorously self-similarity is to realize an experiment such that

$$A^2(t)A'(t)=\pm 1 \text{ so } A(t)=(1\pm 3t)^{1/3} .$$

This occurs when the fluid flux behaves in time like $t^{-1/3}$, which is probably not easy to realize. For the moment, we focus on the selection mechanism of self-similar shapes by a constant effective surface tension. Since the linear geometry is most familiar, we explain in the last section how to transform this free-boundary problem in a wedge into a new free-boundary one in a linear channel.

B. Transformation of the wedge into an infinite strip

The Saffman-Taylor instability, which occurs in an infinite strip, has been extensively studied experimentally [5], numerically [7], and analytically [6,13]. For the physicist, this instability no longer seems mysterious, at least in the steady-state approximation. We are able now to predict both the shape and the growth rate U of steady-state ideal patterns. Even the deviations from ideal situations like three-dimensional effects [14] or inhomogeneity in the fluid [15] (presence of a bubble, a thread, etc.) seem rather well understood. For this geometry, time-dependent situations which occur at very low surface tension (or large pushing velocity) form the only remaining challenge [1,11,16]. Moreover, the experiment in a wedge and the associated DLA simulations indicate some continuity of the physical results, at least for values of the angle not too large. As an example, *at low angles,* the shape of the experimentally selected finger is not very different from the Saffman-Taylor solution with the same λ parameter once modified by the following conformal map:

$$z=\frac{2}{\theta_0}\ln(z_1) . \tag{2.6}$$

In the following we will call the infinite strip the Π plane and Π_1 the physical plane. Moreover, there exist a continuum set of self-similar solutions [12] in the absence of surface tension parametrized by the relative width λ which varies from zero to one, at least for $-\pi\le\theta_0\le\pi/2$. Among this double-continuum set of solutions (indexed by both λ and θ_0) the steady-state patterns of the linear geometry are no more than the restriction for $\theta_0=0$. Finally the λ parameter, selected either experimentally or by the DLA simulations [11], deviates quite linearly in θ_0 from the well-known 0.5 value, at vanishing surface tension. All these reasons indicate a continuous behavior: this is why we have decided [12] to recover the linear geometry instead of the wedge one, via the conformal map [Eq. (2.6)].

Figures 1(a) or 1(b) and 1(c) show the corresponding characteristic points in the two planes: ED means the upper wall, A indicates either the tail of the convergent finger or the origin of the petal in the divergent flow regime. The nose B of the finger fixed at (1,0) in the Π_1 plane becomes our frame origin in the Π plane. The center of the sector is sent either at $+\infty$ (for the convergent flow) or $-\infty$ otherwise. The two walls ED and $E'D'$ are parallel and distant from two length units. Our notation is that of Ref. [7]. In the Π plane, the velocity potential remains Laplacian and the walls plus the center line BC (C is at infinity) are always stream lines. Anyway one has to adapt the boundary conditions on the interface: Eqs. (2.3) and (2.4). This adaption is easiest if one introduces first polar coordinates: r_1 and θ_1 in the Π_1 plane. With these coordinates, the normal gradient is

$$\mathbf{n}_1\cdot\nabla_1\phi=\left[\mathbf{r}_1\frac{d\theta_1}{ds_1}\frac{\partial\phi}{\partial r_1}-\frac{dr_1}{ds_1}\frac{1}{r_1}\frac{\partial\phi}{\partial\theta}\right]\epsilon(\pi-\theta)$$

with $ds_1=(dr_1^2+r_1^2d\theta_1^2)^{1/2}$ and $\epsilon(x)$ the sign of x. Since the polar coordinates are simply related to z via Eq. (2.6):

$$x=\frac{2}{\theta_0}\ln(r_1),\quad y=\frac{2\theta_1}{\theta_0}$$

we deduce without any difficulty the velocity continuity equation in the Π plane:

$$\mathbf{n}\cdot\nabla\phi=\frac{|\theta_0|r_1}{2}\mathbf{n}_1\cdot\nabla_1\phi=\frac{|\theta_0|}{2}\exp(\theta_0 x)\cos(\Theta) \tag{2.7}$$

with Θ the angle in the Π plane between the interface normal and the x axis [see Fig. 1(c)]. As expected, this quantity is always positive since $-\pi/2\le\Theta\le\pi/2$. The curvature in polar coordinates is given by

$$\Omega_1=\frac{2r_1'-r_1r_1''+r_1^2}{(r_1^2+r_1'^2)^{3/2}}\epsilon\left[\frac{dx}{d\theta}\right] .$$

r' (r'') means the first (second) derivative with respect to the polar angle θ_1. These derivatives can be written in terms of x and y and we get

$$\Omega_1=\frac{2}{|\theta_0|}\exp(-\theta_0 x/2)\left[\frac{y''}{(1+y'^2)^{3/2}}-\frac{\theta_0}{2}\frac{|y'|}{(1+y'^2)^{1/2}}\right]$$
$$=\frac{2}{|\theta_0|}\Omega_\theta . \tag{2.8}$$

Henceforth we do not need the intermediate polar coordinates so y' and y'' mean the derivatives with respect to x. We deduce the Laplace equation in the Π plane:

$$\phi-\phi_0=-2\sigma|\theta_0|\Omega_\theta \tag{2.9}$$

with σ the effective surface tension parameter given by

$$\sigma=\frac{b^2}{12\mu}\frac{T}{A(t)R_0^3}\frac{1}{\theta_0^2}=\frac{b^2}{12\mu}\frac{T}{U(t)[R_1(t)]^2}\frac{1}{\theta_0^2}$$

with $U(t)$ and $R_1(t)$ the instantaneous velocity and position of the nose finger in the physical plane Π_1. Note that this quantity has been measured in Refs. [1] and [9] during the growth experiment. The rescaling of ϕ by $|\theta_0|/2$ shows that the classical ST instability in the linear geometry is a particular case corresponding to $\theta_0=0$ and to asymptotic long times. If the fluid flux decreases with time as $t^{-1/3}$, σ is no longer time dependent and is only related to the finger position at time $t=0$. In this case, it reads

$$\sigma=\frac{b^2}{12\mu}\frac{T}{R_0^3}\frac{1}{\theta_0^2}\ .$$

Now we know the equations in the Π plane. As it is usual now, let us transform the free-boundary problem in the Π plane in a unique equation for the interface suitable for the numerics.

III. INTEGRO-DIFFERENTIAL EQUATIONS FOR THE INTERFACE

A. The Green's-function formulation

We are ready now to establish the integro-differential equation for the interface since we know the Green's function of a Laplacian field in an infinite strip. When the profile is symmetric, it reads

$$G(M,M_0)=-\tfrac{1}{2}(x_0-x)h(x_0-x)-\frac{1}{4\pi}\ln(\lambda_-)+\text{c.c.} \tag{3.1}$$

with $\lambda_\pm=1-\exp[-\pi|x-x_0|+i\pi(y_0\pm y)]$, $h(x)=1$ for positive arguments x and $h(x)=0$ otherwise.

The velocity potential ϕ on the interface satisfies

$$\frac{\phi_{\text{int}}-\phi_0}{2}=-\int dS\, G\mathbf{n}\cdot\nabla\phi+\int dS(\phi_{\text{int}}-\phi_0)\mathbf{n}\cdot\nabla G \tag{3.2}$$

with dS the profile arclength. Let us transform this equation into a form more suitable for numerical purposes:

$$4\sigma\Omega_\theta[1-y(x_0)]-\int_{-\infty}^{x_0}dx(y-\lambda)\exp(\theta_0x)[1+\theta_0(x-x_0)]+4\sigma\int_{-\infty}^{x_0}dx\,y'\Omega_\theta-\frac{1}{4\pi}[Z_++Z_-+(Y_+-Y_-)+\text{c.c.}]=0\ , \tag{3.3}$$

$$Z_\pm=\int_{-\infty}^{0}dx\,y'\exp(\theta_0x)\ln(\lambda_\pm),\quad Y_\pm=i4\sigma\int_{-\infty}^{0}dx\frac{d\Omega_\theta}{dx}\epsilon(x-x_0)\ln(\lambda_\pm)\ .$$

We introduced these notations in a previous paper concerning directional solidification at low velocities [17]. In this case, the Green's-function case is rather close to the viscous-fingering one: we only have to adapt the boundary conditions. In [17], we have explained extensively our numerical procedure and our algorithm which here is appreciably more simple. The numerical algorithm is iterative and requires a starting function. Most of the time, we have chosen the ST analytical profile [4]:

$$y(x)=\pm\frac{2\lambda}{\pi}\arccos\left[\exp\left[\frac{\pi x}{2(1-\lambda)}\right]\right]\ . \tag{3.4}$$

We can modify this choice at large σ or θ_0 because the iterative scheme diverges. At large σ, we use the description given by Dombre and Hakim [18] in terms of the pendulum function. Ideally, we could also use as a starting shape the exact analytical expression of the family of solutions at $\sigma=0$. In the Π_1, they have the rather complicated form [12]

$$x_1=\epsilon(\theta_0)s^{\theta_0(1-\lambda)/2\pi}F\left[\frac{\theta_0(2-\lambda)}{2\pi},-\frac{\lambda\theta_0}{2\pi},\tfrac{1}{2},1-s\right],$$

$$y_1=As^{\theta_0(1-\lambda)/2\pi}(1-s)^{1/2}\times F\left[\tfrac{1}{2}+\frac{\theta_0(2-\lambda)}{2\pi},\tfrac{1}{2}-\frac{\lambda\theta_0}{2\pi},\tfrac{3}{2},1-s\right],$$

with

$$A=2\tan\left[\frac{\lambda\epsilon(\theta_0)\theta_0}{2}\right]\times\frac{\Gamma(1-\theta_0(2-\lambda)/2\pi)\Gamma(1+\lambda\theta_0/2\pi)}{\Gamma(\frac{1}{2}-\theta_0(2-\lambda)/2\pi)\Gamma(\frac{1}{2}+\lambda\theta_0/2\pi)} \tag{3.5}$$

with F a hypergeometric function and Γ the gamma function. s is restricted to [0,1]. Do not forget that this set has to be transformed following Eq. (2.6) before the numerical integration. In any case, at large values of the sector angle, numerical problems occur due mainly to the presence of the exponentials: $\exp(\theta_0x)$ in the integrand. Finally, one can determine the asymptotic shape of the finger in the tail by a careful analysis of Eq. (3.3) (see the Appendix). The derived algorithm does not need the asymptotic expansion. This is probably why it is less efficient for large angles where the exponentials are the natural cutoff of the integrals.

The Green's-function technique is one way to transform a free-boundary problem in a unique integro-differential equation for the profile. Although very complicated and impossible to solve analytically except for some asymptotic values of parameters, this equation is really an improvement and allows numerical treatments. Nevertheless, for Laplacian systems, the conformal map [4] and the hodograph method, first introduced by Mclean and Saffman (MS) for the viscous-fingering problem [7], represent *a priori* an alternative way to transform a free-boundary problem. In the next section, we

explain how to apply this method to the viscous fingering in a wedge.

B. The hodograph method

Since the extension of this method to our case is not obvious, we recall here the strategy of this method applied first for the linear geometry and show how it can be extended to any geometry. Note that this method especially requires Laplacian fields. For $\theta_0=0$, once rescaled, the equation for the normal velocity (2.7) is

$$\mathbf{n}\cdot\nabla\phi=\cos(\Theta)=\frac{\partial\psi}{\partial s} . \tag{3.6}$$

Equation (3.6) introduces the stream potential ψ which is the imaginary part of a generalized complex potential Φ. Both the real (ϕ) and imaginary (ψ) parts of Φ satisfy the Laplace equation. We recall the boundary conditions on the walls and at infinity:

$$\phi\approx\begin{cases}0 & \text{when } x\to-\infty \text{ and } \lambda<|y|<1\\ \lambda x & \text{when } x\to\infty \text{ and } -1<y<1\end{cases},\qquad \frac{\partial\phi}{\partial y}=0 \text{ for } y=\pm1 . \tag{3.7}$$

Here, these equations are dimensionless. Mclean and Saffman [7] have introduced an analytical function whose imaginary part vanishes on the finger. In the linear geometry, this function is easily found:

$$\Phi^*=\frac{\Phi-z}{1-\lambda} . \tag{3.8}$$

Note that the center line BC and the finger are stream lines ($\psi^*=0$) and, because of the normalization, so are the walls $y=\pm1$ with $\psi^*=\pm1$. Φ^* has an obvious physical meaning: it is the velocity potential in the frame of the finger but, for the following, its *main* interest is to transform the finger into a stream line. The MS method then consists of eliminating the walls by transforming half of the infinite strip in an upper-half Σ space. Σ is given by

$$\Sigma=s+it=\exp[(\phi_0^*-\Phi^*)\pi] . \tag{3.9}$$

ϕ_0^* is the potential at the nose. Since the unknown finger has been transformed into the stream line $\psi^*=0$, it is located on the segment $s\in[0,1]$. The center line, which is also a stream line, occupies half of the line $1<s<\infty$, and the upper wall ($\psi^*=-1$) occupies the negative s axis $-\infty<s\le0$. All the remaining treatment is a matter of algebra, the keypoint being the localization of the unknown interface in the Π plane on a segment of the real axis in the Σ plane. The extension of the MS method to arbitrary geometry seems to present serious difficulties due to the continuity equation [Eq. (2.7)]. This is only true in appearance. Let us construct an analytical function of z, $H(z)$, whose imaginary part on the unknown finger is given by

$$\mathrm{Im}[H(z)]=\int_0^S dS'\exp(\theta_0 x)\cos(\Theta)=\int_0^S dS'\exp(\theta_0 x)\frac{dy}{dS'} . \tag{3.10}$$

S is the curvilinear positive coordinate defined on the finger, from the nose. Moreover, we will impose the condition that $\mathrm{Im}[H(z)]$ vanishes on the center line and is a constant on the wall: Q_0/λ. Here, Q_0 (which is dimensionless) represents half the fluid flux across the interface. It is equal to λ for the linear cell:

$$Q_0=\int_0^\infty dS'\exp(\theta_0 x)\cos(\Theta) . \tag{3.11}$$

We also construct a generalized potential which transforms the finger into a stream line

$$\Phi^*=\frac{\Phi-H(z)}{(1-\lambda)Q_0/\lambda} . \tag{3.12}$$

We recover the same situation as above [Eq. (3.8)] and we will follow exactly the same strategy: the conformal map from Π to Σ. The only difference comes from the absence of physical meaning for the generalized potential and of a closed-form analytical expression for $H(z)$ which makes the following algebra a little more complicated.

Let us first write the Laplace equation (2.8) and (2.9) in terms of Φ^*:

$$\frac{\partial\phi^*}{\partial S}=-\frac{1}{(1-\lambda)Q_0/\lambda}\left[\sigma\frac{\partial\Omega_\theta}{\partial S}+\frac{\partial\,\mathrm{Re}(H)}{\partial S}\right]=\frac{q}{(1-\lambda)} . \tag{3.13}$$

As in [7], we have introduced the analytical function:

$$\frac{d\Phi^*}{dz}=\frac{q}{1-\lambda}\exp[i(\Theta+\pi/2)] .$$

In the linear geometry, it represents the complex fluid velocity. We calculate $\mathrm{Re}(H)$ using the Cauchy integral theorem, taking advantage of the fact that $\mathrm{Im}[H(s)-(Q_0/\lambda)h(-s)]$ vanishes for every real s value outside [0,1]. We deduce, without any difficulty, that

$$\frac{\partial\,\mathrm{Re}(H)}{\partial s}=\frac{Q_0}{\lambda\pi s}-\frac{1-\lambda}{\pi^2 s}\mathrm{P}\int_0^1 dt\frac{\exp(\theta_0 x)\cos(\Theta)}{q(t-s)} \tag{3.14}$$

since $dS=-ds(1-\lambda)/\pi qs$. P denotes the principal value of the integral. Now, we define $\tau=\Theta-\pi/2$ in order to use the same notations as [7] and we derive from the Laplace equation the integro-differential equation of this free-boundary problem:

$$\kappa qs\frac{\partial}{\partial s}\exp\left[-\frac{\theta_0 x}{2}\right]\left[qs\frac{\partial\tau}{\partial s}+\frac{\theta_0}{2\pi}(1-\lambda)\sin(\tau)\right]-q=\frac{-q}{1-\lambda}-\frac{q}{\pi Q_0/\lambda}\int_0^1 dt\frac{\exp(\theta_0 x)\sin(\tau)}{q(t-s)} \tag{3.15}$$

with $\kappa=4\pi^2\sigma/(1-\lambda)^2Q_0/\lambda$ and the following boundary conditions: $\tau(0)=0$, $\tau(1)=-\pi/2$, $q(0)=1$, and $q(1)=0$.

This equation relates three unknown functions: q, τ, and x. We need two other equations which have already been given in [7]. Since $q\exp[-i(\tau-\pi)]$ is an analytical function of z, the Cauchy integral equation relates $\ln(q)$ and τ:

$$\ln(q)=-\frac{s}{\pi}\int_0^1 dt\frac{\tau(t)}{t(t-s)} . \tag{3.16}$$

Here also we use the fact that $\tau(s)$ vanishes everywhere on the real s axis, except for $s\in[0,1]$. The other relation simply indicates that z is a function of any analytical function so of Φ^*.

$$x(s)+iy(s)=-\frac{1-\lambda}{\pi}\int_s^1 dt\frac{\exp(i\tau)}{tq} . \tag{3.17}$$

The reader can check that we recover the MS equations for $\theta_0=0$. In this case, the set is reduced to two coupled equations. In the radial geometry, one has to solve three coupled equations: one which is integro-differential plus two integral equations, so the algorithm is a little more complicated. Nevertheless, the code built on this method remains more effective than the Green's function. Although, with the hodograph method, for $\kappa=0$, we succeed in finding analytical solutions [12], we do not give here the analytical expression for q and τ, which are much too complicated and not necessary for the following.

IV. THE NUMERICAL RESULTS COMPARED TO THE EXPERIMENT

A. Numerical results without surface tension

It does not seem necessary to come back to the derivation of the analytical solutions [Eq. (3.5)] which are the subject of a separate publication [12]. Let us recall that this set of continuous solutions [Eq. (3.5)] both in λ and θ_0 have been found with the hodograph method. The analytical shapes (Fig. 1 displays some examples) have been compared to the numerical one, obtained with the two codes. Note that only the Green's-function code can give a complete independent proof since it rests on a different method. A more precise test is the study of the definition range since this treatment reveals a lower bound for $\lambda=2-\pi/\theta_0$ for divergent flow and $\theta_0>90°$ and an upper bound for convergent flow and $\theta_0<-180°$: $\lambda=-\pi/\theta_0$. These restrictions are derived mathematically from Eq. (3.5) (the Γ functions cannot have a negative argument) but another class of solutions forgotten in [12] can appear. So it seems important to study these limits. With the Green's-function code, one way to get solutions in the forbidden ranges consists in relaxing the condition of vanishing first derivative at the tip, in the hodograph code in relaxing $\tau=-\pi/2$ at the tip. Figure 2 shows that the verification of these bounds was possible only for a few sector angles since these limits are not always easy to reach numerically. The reader may wonder about the physical significance of these restrictions for the selection. In fact we will show that the selected λ at low surface tension is much lower than the upper bound for convergent flow and much larger than the lower bound for the divergent flow, so these limits will not perturb the selection by surface tension. One can wonder too what happens for sector angle greater than 180° in divergent flow. The experiment, for example, Refs. [1] and [2], gives the answer by showing that the pattern splits into several fingers in order to give an effective wedge angle much smaller than the physical one.

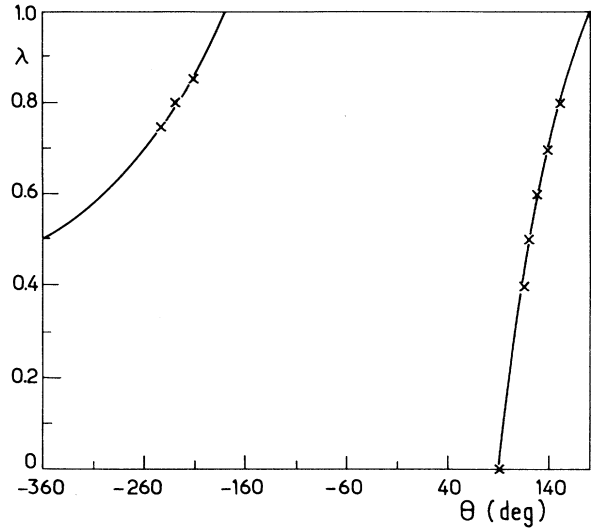

FIG. 2. Domain of existence of self-similar profiles. Crosses indicate numerical verifications.

B. Numerical results at low surface tension

1. *The stable convergent flow regime*

The convergent flow spectrum appears rather classical (see Fig. 3). For a given sector angle $\theta_0=-20°$, the different eigenvalues λ_n increase monotonously with the surface tension σ. When compared to the linear case, it seems that only the first eigenvalue is affected by the geometry. It is shifted from $\lambda_{\min}=0.5$ ($\theta_0=0$) to $\lambda_{\min}=0.42$ ($\theta_0=-20°$), values obtained for arbitrary small σ. The eigenvalues λ_n ($n>1$) corresponding to unstable fingers seem less modified (see Fig. 3), a result we have noticed before for the linear case with an anisotrop-

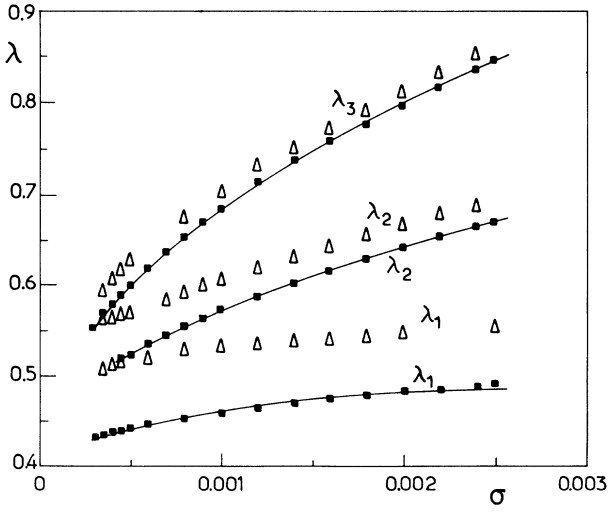

FIG. 3. Three computed eigenvalues, $\lambda_1,\lambda_2,\lambda_3$, vs the effective surface tension parameter σ: ■ for $\theta_0=-20°$; △ for $\theta_0=0°$.

ic surface tension. Nevertheless, it is likely that the different eigenvalues λ_n split from a common λ_{min} value which is θ_0 dependent. The first eigenvalue λ_1 ($\theta_0=-20°$) behaves unambiguously like $\kappa^{2/3}$ [given by Eq. (3.15)], as λ_1 ($\theta_0=0°$) the well-known scaling of the linear geometry [7].

The comparison with the experimental result is very satisfactory. Let us focus first on the evolution of λ_{min} with the sector angle. At fixed surface tension $\sigma=0.001$, the λ spectrum, as a function of θ_0, decreases slowly when $|\theta_0|$ increases [see Fig. 4(a)]. The width $\lambda(\theta_0)$ at small σ is "quasilinear" in θ_0 for small angles [Fig. 4(b)], the approximate slope is of order 0.003/deg, a value close to the experimental one 0.0032/deg (crosses in Figs. 4(a) and 4(b) and Ref. [1]); the averaged DLA gives 0.0034/deg. The fit is better when the sector angle is not too large in the convergent flow case. This comes from the difficulty in obtaining centered fingers when the wedge is large [19]. Numerically, at large angles, the behavior departs from linearity, a result not observed experimentally [1,11]. The absence of singularity in the spectrum [Figs. 4(a) and 4(b), for negative θ_0 values] and the low selected values λ explains why the experimental finger seems more stable in this geometry. If one assumes the stability analysis of the Saffman-Taylor finger [8] to be also valid for the viscous fingering in a wedge, one imagines that only the first level is stable. This is consistent with the fact that the levels $n=1,2,3$ are further apart from each other so that noise does not induce a jump from the stable level to the unstable ones. For a given intermediate value of the sector $\theta_0=-23°$, the agreement between the calculated first eigenvalue λ_1 and the experiment is rather good if one examines Fig. 5. A very slight discrepancy remains at small σ values. Figure 5 shows that the only eigenvalue relevant for experimental considerations is the first one as for the linear geometry. Note that the experimentalists have made a rather difficult measurement of the instantaneous values of the parameter σ (called B in their paper). This measurement is rather uneasy at low σ which corresponds to fast fingers.

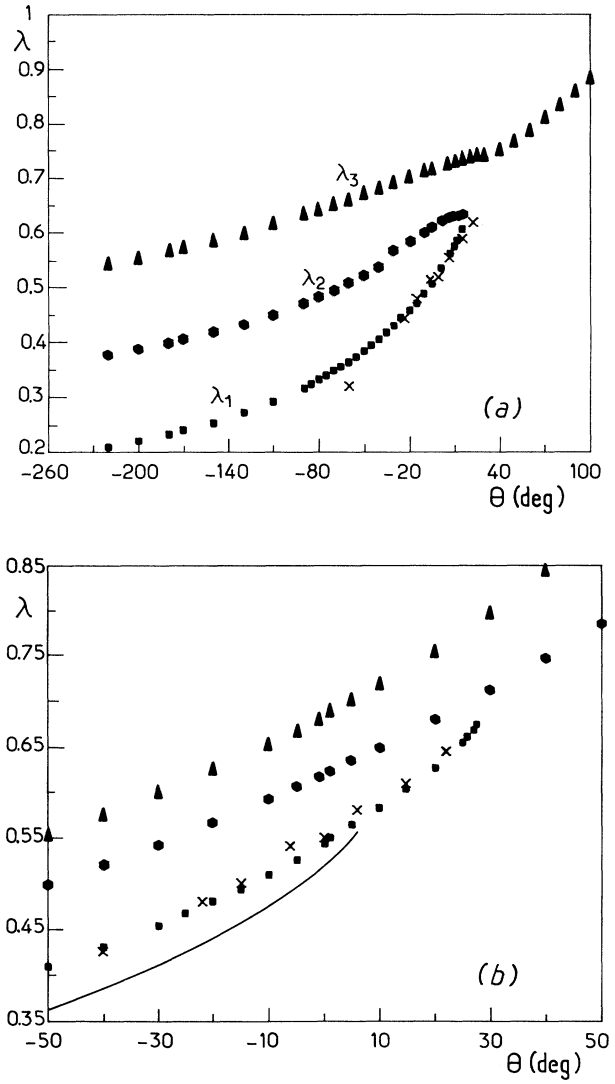

FIG. 4. (a) Three relative widths, $\lambda_1,\lambda_2,\lambda_3$, vs the wedge angle for convergent and divergent flow, at fixed effective surface tension parameter $\sigma=0.001$. Crosses ($\times$) indicate experimental measurement [1]. (b) Quasilinear behavior of the first eigenvalue λ_1 vs the wedge angle θ_0 for various fixed surface tension parameters σ. ——, $\sigma=0.0004$; ■, $\sigma=0.002$; ●, $\sigma=0.01$; ▲, $\sigma=0.02$. Crosses ($\times$) are experimental measurements at $\sigma=0.002$ [10].

2. *The divergent flow and the origin of tip-splitting*

The most amazing numerical result is the presence of a loop at fixed effective surface tension parameter σ in the graph $\lambda=f(\theta_0)$, for divergent flow as shown in Fig. 4(a). This loop is characteristic of the divergent flow regime ($\theta_0>0$), since it does not exist in the convergent flow regime [Fig. 4(a), $\theta_0<0$] and in the traditional linear geometry ($\theta_0=0$). It means that, at low and fixed surface

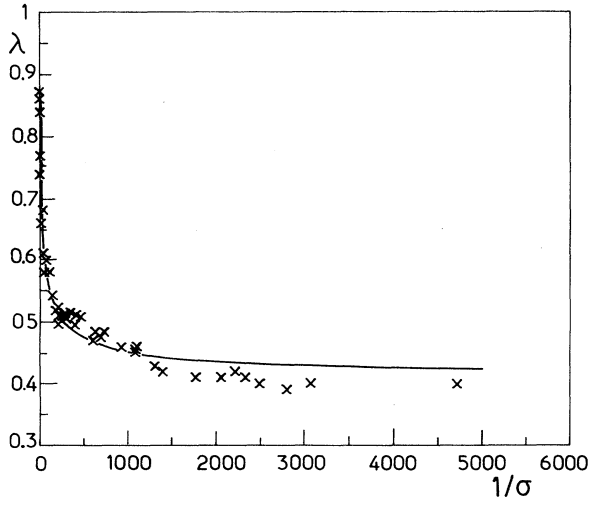

FIG. 5. Comparison between predicted and measured relative width λ vs the capillary "experimental" parameter $1/\sigma$ for $\theta_0=-23°$: ——, numerical values; $\times$, experimental results [1].

tension, when the sector angle becomes too large, two levels disappear: the first and second ones. As discussed later, it will be responsible for the tip-splitting instability. This loop occurs at low σ and seems to disappear for $\sigma > 0.005$, at least for $\theta_0 \leq 90°$ (see Fig. 6). Results for the largest values of θ_0 are very difficult to obtain, because of the very high values of the selected λ: $\lambda \geq 0.90$. This loop couples the first and second levels, if one refers to the ordinary ST eigenvalue spectrum, while the third level seems to be not too much affected by the opening of the sector. It is shifted toward large angles when σ increases. As soon as σ is greater than 0.005, the plot $\lambda = f(\theta_0)$ [Fig. 4(b)] is "quasilinear" in θ_0. At fixed sector angle, the $\lambda = f(\sigma)$ spectrum recovers the same looping phenomena as shown by Figs. 7 (for $\theta_0 = 20°$) and 8 (for $\theta_0 = 90°$). Concerning the right-angle geometry (for $\theta_0 = 90°$), a WKB analysis [10] gave $\lambda_{\min}(\theta_0) \approx 0.85$ in good agreement with Fig. 8, which indicates 0.858 for the loop $\lambda_{3,4}$; however, this WKB analysis had not detected the presence of loops.

Let us focus, for the moment, on the first and second eigenvalues perfectly defined at high surface tension (the right part of Figs. 7 and 8). There is a characteristic threshold of surface tension which depends on the sector angle $\sigma_{1,2}(\theta_0)$. Below this threshold, the first and second eigenvalues λ_1 and λ_2 do not exist. Above it, they separate together from a common value $\lambda_{1,2}(\theta_0)$. So it is a kind of bifurcation with a nonvanishing surface tension threshold. A more careful numerical analysis at lowest surface tension "indicates" that the other eigenvalues show the same feature: that is, existence of a threshold $\sigma_{n,n+1}$ (n is odd). Below this threshold, the eigenvalues λ_n and λ_{n+1} do not exist mathematically, at the threshold they have a common value $\lambda_{n,n+1}$, above, they split into two different levels n and $n+1$. Our intuition is that this phenomenon occurs for any divergent flow and any eigenvalue but it is not always easy to show numerically this scenario. As shown in Fig. 6, the threshold $\sigma_{1,2}$ is an increasing function of the sector angle, and we can extend this result to any threshold $\sigma_{n,n+1}$ as suggested by the comparison of two sector angles $\theta_0 = 20°$ and 90°. Probably $\sigma_{n,n+1}$ is less than $\sigma_{m,m+1}$ if n is greater than m. Our predictions concerning levels higher than the first two require confirmation by a very careful WKB analysis, which is the most suitable treatment at extremely low surface tension. Probably, the results of analytical solutions (3.5) without surface tension will make this analysis

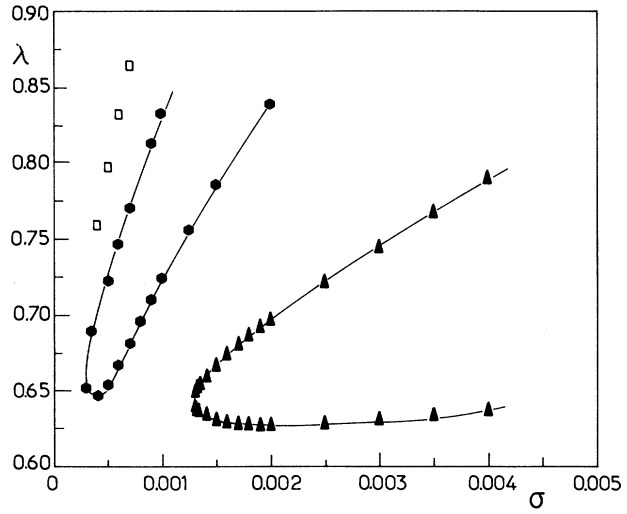

FIG. 7. Eigenvalues spectrum vs σ at fixed sector angle $\theta_0 = 20°$. ▲, first and second levels; ●, third and fourth coupled levels; □, a fifth incomplete one.

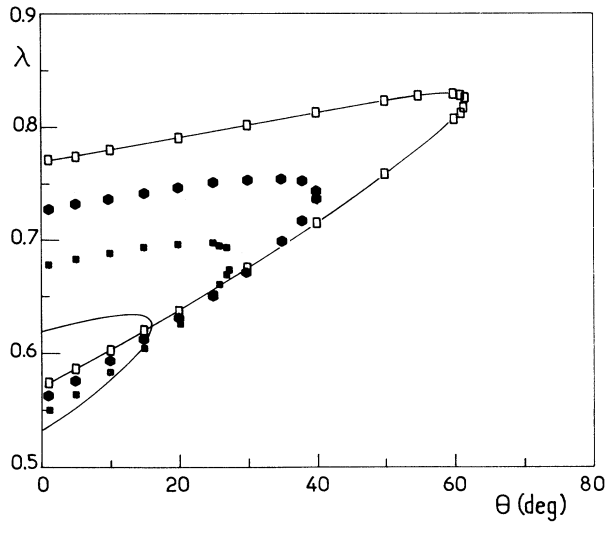

FIG. 6. Relative widths λ_1 and λ_2 of the petal finger in divergent flow vs the sector angle θ_0, for various effective surface tension parameters σ: the loop phenomena. Eigenvalues: λ_1 (the lower curve) and λ_2 (the upper curve) for $\sigma = 0.001$ (——), $\sigma = 0.002$ (■), $\sigma = 0.0003$ (●), $\sigma = 0.0004$ (□—□—□).

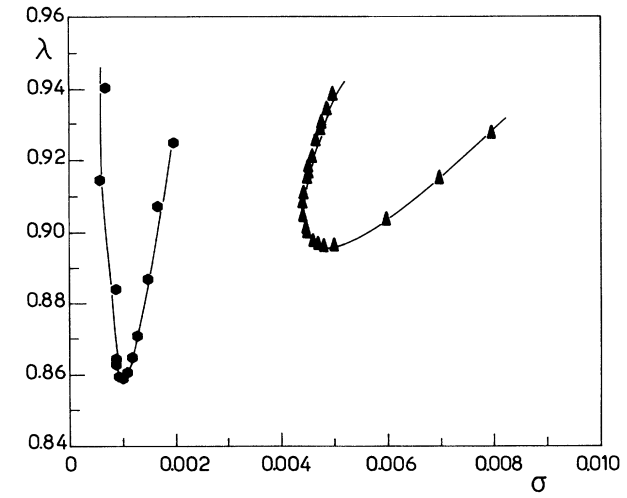

FIG. 8. Eigenvalues spectrum vs σ at fixed sector angle $\theta_0 = 90°$. ▲, first and second levels; ●, third and fourth coupled levels.

possible. At very low surface tension, the numerical values are very sensitive to the grid, which also acts like an anisotropy in the same way as in the experiment. So the calculated λ values in this regime are lower than the real ones. In good cases, it has been possible to reach σ values of order 0.0003 and 0.0004 with the hodograph code and 150 mesh points but this is really our ultimate limit. Within this context, the reader can imagine the difficulty in obtaining numerically the vicinity of the loops for higher eigenvalues than $\lambda_{1,2}$. In any case, the two codes give the same results and offer strong evidence for the existence of these loops.

Experimentally, it had also been observed [1] that the finger lost its stability at a limiting value of σ, increasing with θ_0. If one assumes that only the first level is stable, this stable solution disappears at the loop, for $\sigma=\sigma_{1,2}$. So we can imagine the following scenario for the experimental dynamics where the finger grows at constant velocity. As time passes, the effective surface tension $\sigma(t)$ decreases because the channel width increases. The observed petal finger shows a relative width $\lambda(t)$, which slightly decreases following the stable branch λ_1, as shown in Fig. 7 for $\theta_0=20°$. When its shape has a λ very close to $\lambda_{1,2}(\theta_0)$, it becomes unstable and tends to split into two petal fingers. Afterward, sometimes, it is characterized by an effective sector angle, the value of which is half the experimental one. For this half sector value, the petal finger recovers stability: as the angle is smaller, its new characteristic σ is larger. Furthermore, at this angle the instability threshold $\sigma_{1,2}$ is smaller. In other terms, tip-splitting reduces the radius of curvature at the nose, so increases the stabilizing effect of the capillarity. This scenario can be used to interpret the first tip-splitting events in a radial growth experiment. Let us recall that, at the first stages of growth, radial fingering patterns [2] show independent fingers that seem to grow in their own virtual sector (for a detailed discussion between sector constrained growth and unconstrained radial growth see [1]). The number of independent fingers cannot be exactly predicted. It seems to depend on the initial growth conditions and varies from 5 to 7. Tip-splitting of the fingers occurs as soon as the tip radius is too large, so many times in the growth process, giving rise to a ramified structure. Rauseo, Barnes, and Maher [2] realized the first quantitative and statistical analysis of this structure, in order to characterize their patterns. It is possible at long times after many tip-splitting events. In connection with this, Sarkar [3] recently has imagined a cascade of successive tip-splitting instabilities in radial growth, as soon as the tip finger has a width related to its velocity by Eq. (1) of Ref. [3]:

$$R(t)=qU(t)^{-1/2} . \tag{4.1}$$

Clearly, this q value is proportional to our $\sigma_{1,2}(\theta_0)$. So as soon as the tip radius reaches the above value, it splits in three equal parts, and the extreme parts of the pattern instantaneously grow while the middle one is inhibited. When the extreme parts show the same behavior as given in Eq. (4.1), they split again and this scheme happens repeatedly. Neglecting what happens just after a bifurcation, we deduce scaling laws for the average geometry after n bifurcations. Our numerical study confirms this starting point: that is, existence of this constant q but it shows also that it cannot be taken as a constant during the cascade process. First, it depends on the fictitious sector value which is reduced after any bifurcation. A WKB treatment [19] valid for small values of θ_0 reveals that $\sigma_{12}(\theta_0)\approx\theta_0^{3/2}$. This prediction is approximately verified for arbitrary θ_0 values less than 70° providing that one changes $\sigma_{12}(\theta_0)$ in $\kappa_{12}(\theta_0)$ following Eq. (3.15) since the proportionality between $\sigma_{12}(\theta_0)$ and $\kappa_{12}(\theta_0)$, valid at low θ_0, is lost when the sector angle increases. Second, the finger after a cascade is no longer centered in the fictitious sector. Finally, the self-similarity is perhaps much more questionable after tip-splitting. Maybe these restrictions are only details in the Sarkar model which mainly focuses on statistical aspects of the radial geometry after a large number of bifurcations by tip-splitting.

3. *Comparison with the experiment*

This scenario for the explanation of the tip-splitting instability can be compared to the experimental results. In Fig. 9, we have plotted numerical and experimental results of Ref. [1], for $\theta_0=23°$. The agreement between predicted λ_1 and measured λ values is excellent when σ_1 is greater than $\sigma_{1,2}$. So, as time passes, the σ parameter decreases and the time-dependent relative width of the finger $\lambda(t)$ follows closely the first level, which is really the relevant one for the experiment. On the other hand, the global evolution of the instability threshold observed experimentally is well understood by the existence of loops and the finger appears to destabilize at $\sigma_{1,2}$. As the angle θ_0 increases so does the threshold. However, quantitatively there is a slight discrepancy, for instance, when σ (or B) becomes smaller than $\sigma_{1,2}$, Ref. [1] and Fig. 9 indicate a value which cannot be reproduced numerically.

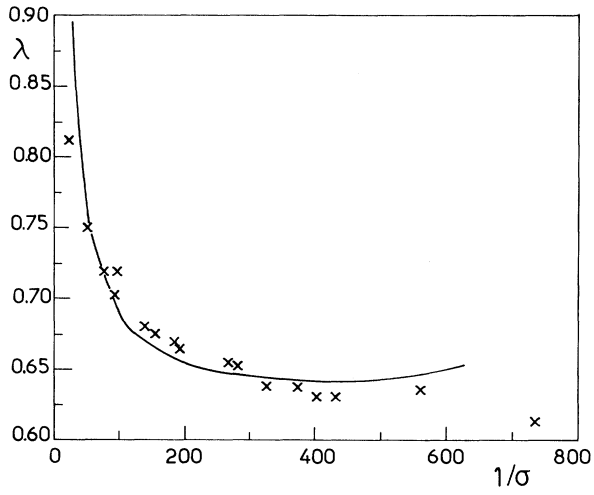

FIG. 9. Comparison between predicted and measured relative width λ vs the capillary "experimental" parameter $1/\sigma$ for $\theta_0=23°$: ——, numerical values; ×, experimental results [1].

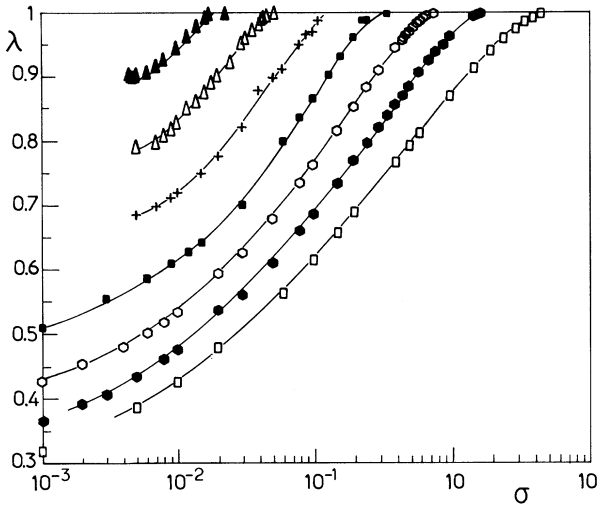

FIG. 10. The selected relative width λ vs σ for various angles. Note that for divergent flow, the curves begin for $\sigma > 0.0005$ (after the loops). ▲, $\theta_0 = 90°$; △, $\theta_0 = 60°$; +, $\theta_0 = 32°$; ■, $\theta_0 = 0°$; ⬡, $\theta_0 = -32°$; ⬢, $\theta_0 = -60°$; □, $\theta_0 = -90°$.

The experimentalist's interpretation [19] for this discrepancy is the following. The experiments are performed with a constantly decreasing σ. It is difficult to detect the first deformation of the finger tip so it is only for a finite disturbance that the instability is noted, as it is seen too late it corresponds to a too small σ. The same discrepancy is seen for several angles in Table I of Ref. [1] and Fig. 6. It is also possible that the dynamics at high growth rate is much more complicated than our "adiabatic model." In any case, we will keep in mind the good agreement for $\sigma > \sigma_{1,2}(\theta_0)$ as shown also by Figs. 4 and 9.

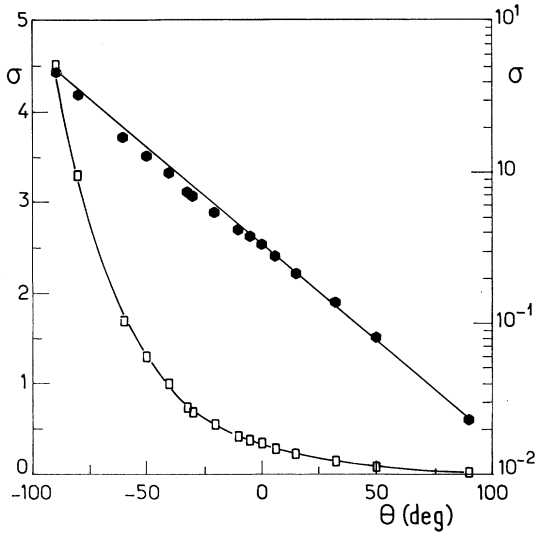

FIG. 11. The extremal surface tension parameter σ vs the sector angle θ_0 for divergent and convergent flow. The logarithmic scale of the right side indicates an exponential behavior of σ (linear curve on the right side).

C. Numerical results for larger σ

When σ increases and oversteps the looping domain: $\sigma > 0.0005$, the λ spectrum as a function of σ has the usual behavior whatever θ_0 (Fig. 10), except the value of the upper bound $\sigma_{max}(\theta_0)$ which seems to decrease exponentially when θ_0 increases (Fig. 11) [20]. This upper bound, first predicted by Kadanoff, Shraiman, and Pomeau [21] has been determined analytically [18] in the linear geometry: $\sigma_{max}(\theta_0) \approx 0.35$. For this value of surface tension, the finger completely fills the cell so $\lambda = 1$. It corresponds to very strong capillary effects. In the hodograph method, the capillary parameter κ goes to infinity. This explains why, at high surface tension, the Green's-function code is more efficient than the hodograph one, since in the first case, the capillary parameter σ reaches a finite value instead of an infinite value κ for the hodo-

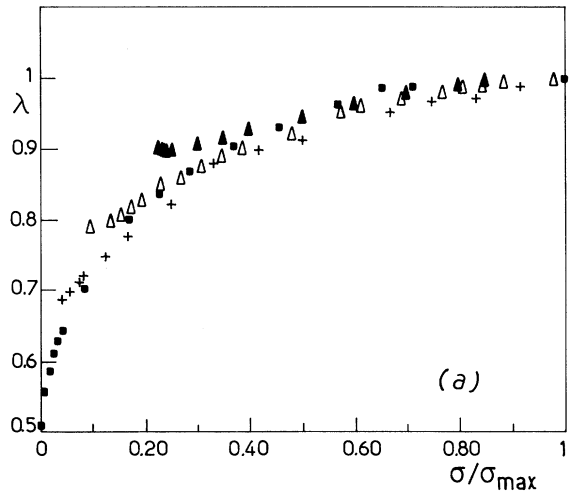

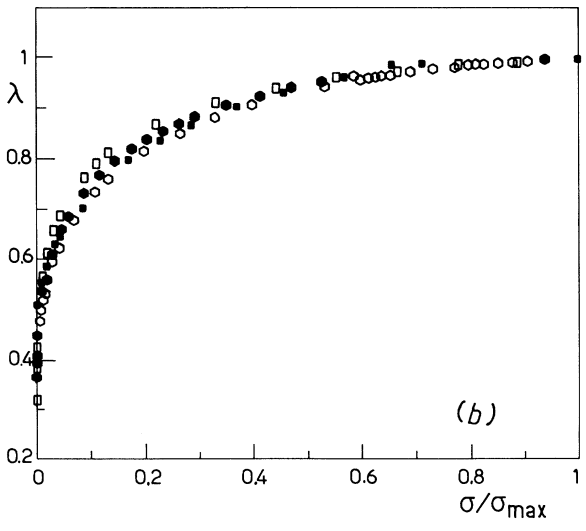

FIG. 12. (a) Universal spectrum $\lambda = f(\sigma/\sigma_{max})$ for any convergent flow. ▲, $\theta_0 = 90°$; △, $\theta_0 = 60°$; +, $\theta_0 = 32°$; ■, $\theta_0 = 0°$. (b) Universal spectrum $\lambda = f(\sigma/\sigma_{max})$ for any divergent flow. ■, $\theta_0 = 0°$; ⬡, $\theta_0 = -32°$; ⬢, $\theta_0 = -60°$; □, $\theta_0 = -90°$.

graph method. For larger values of the surface tension than $\sigma_{max}(\theta_0)$ there are no finger or petal shapes. The numerics indicates an exponentially decreasing behavior of $\sigma_{max}(\theta_0)$ (Fig. 11):

$$\sigma_{max} \approx 0.35 \exp(-a\theta_0) \quad \text{with } a = 0.027/\text{deg} \tag{4.2}$$

but an analytical treatment, perhaps following [18], remains to be done. The common behavior shown by Fig. 10 for arbitrary θ_0 values between $-90° \le \theta_0 \le 90°$ suggests a new plot: $\lambda = g[\sigma/\sigma_{max}(\theta_0)]$. Clearly, at very low surface tension, what one can call the WKB range of σ parameter, one cannot expect a universal behavior and a superposition of the different plots for any θ_0: first because of the dependence of $\lambda_{min}(\theta_0)$ in terms of θ_0, second because of the loop observed for divergent flow. But as soon as one oversteps this WKB regime, when $\sigma/\sigma_{max}(\theta_0)$ increases, all the curves nicely superimpose as shown by Figs. 12(a) and 12(b). The agreement seems better for convergent flow than for divergent flow, but this is due to some numerical inaccuracy especially for $\theta_0 = 90°$. We hope that it will encourage a theoretical treatment and also new experiments. If one takes into account (4.2), one notices that the upper bound for σ has an especially low value for $\theta_0 > 90°$. Moreover σ must be greater than σ_{12} in order to select observable patterns. A good estimate for σ_{12} is about 0.005,0.006 as soon as $\theta_0 > 90°$. Noticing that σ_{12} must be less than σ_{max}, we conclude that this instability with a unique petal cannot be observed for $\theta_0 > 150°$, a value in agreement with the experimental observation and the DLA finding [11] $\theta_0 \approx 144°$.

V. CONCLUSION

This paper is devoted to the selection of self-similar fingers in radial growth over the largest possible domain of surface tension σ and wedge angle values. It shows that for the WKB range of σ values (small values) the selection is specific of any angle but, once this range overstepped, a scaling and universal selection relationship is revealed numerically. In the WKB range of σ values and for divergent flow, the numerics indicate a lower σ bound for the observation of a unique self-similar petal finger. It is the tip-splitting threshold. In convergent flow, it does not occur. At arbitrary low surface tension, very narrow fingers are selected with a relative width which decreases as the wedge angle increases, a result which can be extrapolated up to the complete open geometry: $\theta_0 = -360°$.

Note added. After the completion of this work I received a copy of unpublished work from Yuhai Tu, who explains analytically the results obtained at low surface tension.

ACKNOWLEDGMENTS

This work has been suggested by Y. Couder and V. Hakim. Fruitful discussions with R. Combescot, Y. Pomeau, and M. Rabaud are greatly acknowledged. I am especially grateful to Y. Couder for a critical reading of the manuscript and for fruitful discussions about the experiment. It is a pleasure to thank Y. Couder, V. Hakim, and B. Moussallam for continuous interest and encouragements during the difficult period of computations. The Laboratoire de Physique Statistique is associé au Centre National de la Recherche Scientifique et aux Universités Paris VI et VII.

APPENDIX

1. Asymptotic analysis of the Green's-function equation

As is often the case, we must involve two different situations: with or without surface tension.

a. Asymptotic behavior at vanishing surface tension

Let us assume that in the finger tails, when $|x|$ is large, the profile function in the Π plane behaves like

$$y(x) \approx \lambda - \beta \exp(\mu x) . \tag{A1}$$

To estimate the asymptotic limit of each integral, we will assume that, for large $|x_0|$, the integral is only dominated by the close vicinity of x_0 so, in the integrals, we replace the profile function $y(x)$ approximately by its asymptotic expansion (A1). The first integral in (3.3) is easily estimated and behaves like $[\beta\mu/(\mu+\theta_0)^2]\exp[(\mu+\theta_0)x]$. The estimation of $Z_\pm$ is a little more subtle and we refer to Appendix B of [17]:

$$Z_+ + Z_- = \pi\beta \frac{\mu}{\mu+\theta_0} \left[\frac{2}{\mu+\theta_0} - \cot(\mu+\theta_0) - \frac{\cos[(1-2\lambda)(\mu+\theta_0)]}{\sin(\mu+\theta_0)} \right] \times \exp(\mu+\theta_0) .$$

We deduce without difficulty that

$$\mu = \frac{\pi}{2(1-\lambda)} - \theta_0 . \tag{A2}$$

b. Asymptotic tails in presence of capillary effects

For convergent flow ($\theta_0 < 0$), the curvature in the tail is subdominant compared to each integral involved above, so the asymptotic tail, as given by (A2), remains valid. On the contrary, for divergent flow, integrals involving the curvature are dominant and we need the behavior of $Y_\pm$ (Appendix B of [17]):

$$\mathrm{Re}(Y_+ - Y_-) = -\pi 4\sigma\mu(\mu-\theta_0/2)\beta \left[2(\lambda-1) + \frac{\sin[(2\lambda-1)(\mu-\theta_0/2)]}{\sin[\mu-\theta_0/2]} - 1 \right] \exp(\mu-\theta_0/2) .$$

Once balanced with the first curvature term in Eq. (3.3), we get

$$\mu=\frac{\pi}{2(1-\lambda)}+\frac{\theta_0}{2}\ . \tag{A3}$$

This result is valid for any $\theta_0>0$.

2. Asymptotic behavior of the hodograph method functions

The study of the end-point singularities for $\tau(s)$ and $q(s)$ is absolutely crucial for the derived algorithm, as it has been claimed by Mclean and Saffman. Each computed integral occurring in the hodograph method requires us to take into account these expansions very carefully to give accurate numerical results and to make the algorithm convergent. Anyway, the asymptotic treatment is easier with this formulation compared to the previous one.

a. End-point singularity when $\kappa=0$

We seek a solution about $s=0$ of the form

$$\tau(s)=a_1 s^{\alpha}+a_2 s^{2\alpha}+\cdots\ ,$$

$$q(s)=1+\cdots\ ,$$

$$x(s)=\frac{(1-\lambda)}{\pi}\ln(s)\ ,$$

$$y(s)=\lambda-a_1\frac{(1-\lambda)}{\pi}\frac{s^{\alpha}}{\alpha}\ .$$

The previous coefficient μ is equal to $\mu=\alpha\pi/(1-\lambda)$ (A1). It is not useful here to make an asymptotic analysis of Eq. (3.15) since we know its exact solution, when surface tension is neglected:

$$\exp(\theta_0 x)\sin(\tau)\approx\left[\frac{s}{1-s}\right]^{1/2}$$

and we deduce $\alpha=\frac{1}{2}-\theta_0(1-\lambda)/\pi$ and $\mu=\pi/2(1-\lambda)-\theta_0$, which is in agreement with the result given by the Green's-function technique (A2).

b. End-point singularity with surface tension

The curvature term in Eq. (3.15) occurs in the asymptotic expansion only for $\theta_0>0$. For negative value or convergent flow, the above result (A3) without surface tension has to be maintained. For $\theta_0>0$, the curvature term is greater than $\sin[\tau(s)]$ in the tail of the finger. To balance its contribution, one has to take into account the Hilbert integral in Eq. (3.15). Let us recall the asymptotic expansion of such a Hilbert transform [7]:

$$\int_0^1 dx\frac{x^{\delta}}{x-s}\approx\frac{1}{\delta}+\frac{s}{\delta-1}-\pi s^{\delta}\cot(\pi\delta)+\cdots,\quad s\to 0\ . \tag{A4}$$

This result is valid only for positive δ values less than 1. In this case, the greater term is s^{δ} which is equal to $\delta=\alpha+\pi\theta_0/(1-\lambda)$. Clearly such a contribution cannot be balanced by $s^{\delta'}$ with $\delta'=\alpha-\pi\theta_0/2(1-\lambda)$. So δ is greater than 1. From Eq. (A4), we get for $1<\delta<2$

$$\int_0^1 dx\frac{x^{\delta}}{x-s}\approx\frac{1}{\delta}+\frac{s}{\delta-1}+\frac{s^2}{\delta-2}-\pi s^{\delta}\cot[\pi(\delta-1)]+\cdots,\quad s\to 0\ .$$

The major vanishing contribution is given by the term linear in s which implies $\delta'=1$. So, in the presence of capillary effects and for divergent flow, the asymptotic expansion for $\tau(s)$ is

$$\alpha=1+\frac{\pi\theta_0}{2(1-\lambda)}$$

and for y

$$\mu=\frac{1-\lambda}{\pi}+\frac{\theta_0}{2}\ .$$

We recover the same result as that obtained previously with the Green's-function technique but we note that the $\theta_0=0$ value is singular since we do not recover the MS expansion [7].

[1] H. Thomé, M. Rabaud, V. Hakim, and Y. Couder, Phys. Fluids A **1**, 224 (1989).

[2] J. Bataille, Rev. Inst. Fr. Pet. **23**, 1349 (1968); L. Paterson, J. Fluid. Mech. **113**, 513 (1981); S. N. Rauseo, P. D. Barnes, and J. V. Maher, Phys. Rev. A **35**, 1245 (1987).

[3] S. Sarkar, Phys. Rev. Lett. **65**, 2680 (1990); S. E. May and J. V. Maher, Phys. Rev. A **40**, 1723 (1989); P. Meakin, in *Phase Transitions and Critical Phenomena,* edited by C. Domb and J. L. Lebowitz (Academic, Orlando, FL, 1988), Vol. 12, and references therein.

[4] P. G. Saffman and G. I. Taylor, Proc. R. Soc. London, Ser. A **245**, 312 (1958).

[5] P. G. Saffman, J. Fluid Mech. **173**, 73 (1986); G. M. Homsy, Annu. Rev. Fluid Mech. **19**, 271 (1987).

[6] B. Shraiman, Phys. Rev. Lett. **56**, 2028 (1986); D. C. Hong and J. Langer, *ibid.* **56**, 2032 (1986); R. Combescot, T. Dombre, V. Hakim, Y. Pomeau, and A. Pumir, *ibid.* **56**, 2036 (1986); S. Tanveer, Phys. Fluids **30**, 1589 (1987).

[7] J. W. Mclean and P. G. Saffman, J. Fluid Mech. **102**, 455 (1981); J. M. Vanden-Broeck, Phys. Fluids **26**, 2033 (1983).

[8] D. A. Kessler and H. Levine, Phys. Rev. A **32**, 1930 (1985); D. Bensimon, *ibid.* **33**, 1302 (1986); S. Tanveer, Phys. Fluids **30**, 2318 (1987).

[9] M. Ben Amar, V. Hakim, M. Mashaal, and Y. Couder, Phys. Fluids A **3**, 7 (1991).

[10] E. A. Brener, D. A. Kessler, H. Levine, and W.-J. Rappel, Europhys. Lett. **13**, 161 (1990).

[11] A. Arneodo, Y. Couder, G. Grasseau, V. Hakim, and M. Rabaud, Phys. Rev. Lett. **63**, 984 (1989); Y. Couder, F. Argoul, A. Arneodo, J. Maurer, and M. Rabaud, Phys. Rev. A **42**, 3499 (1990).

[12] M. Ben Amar, Phys. Rev. A **43**, (1991).

[13] D. Bensimon, L. Kadanoff, S. Liang, B. Shraiman, and C. Tang, Rev. Mod. Phys. **58**, 977 (1986).

[14] P. Tabeling, G. Zocchi, and A. Libchaber, J. Fluid Mech. **177**, 67 (1987); P. G. Saffman and S. Tanveer, Phys. Fluids A **1**, 219 (1989); S. Tanveer, in *Growth and Forms: Nonlinear Aspects, NATO Advanced Study Institute, Series B: Physics,* edited by M. Ben Amar, P. Pelcé, and P. Tabeling (Plenum, New York, 1990).

[15] Y. Couder, N. Gerard, and M. Rabaud, Phys. Rev. A **34**, 5175 (1987); G. Zocchi, B. Shaw, A. Libchaber, and L. Kadanoff, *ibid.* **36**, 1894 (1987); D. C. Hong and J. S. Langer, *ibid.* **36**, 2325 (1987); R. Combescot and T. Dombre, *ibid.* **39**, 3525 (1989).

[16] W.-S. Dai, L. P. Kadanoff, and S. M. Zhou (unpublished); S. Tanveer (unpublished).

[17] M. Ben Amar and B. Moussallam, Phys. Rev. Lett. **60**, 317 (1988); M. Mashaal, M. Ben Amar, and V. Hakim, Phys. Rev. A **41**, 4421 (1990).

[18] T. Dombre and V. Hakim, Phys. Rev. A **36**, 2811 (1987).

[19] R. Combescot and M. Ben Amar, Phys. Rev. Lett. **67**, 453 (1991).

[20] Y. Couder (private communication).

[21] L. Kadanoff and B. Shraiman (unpublished); Y. Pomeau, Stud. Appl. Math **73**, 75 (1985).